Denoising and Multiple Tissue Compartment Visualization of Multi-b-valued Breast Diffusion MRI

Ek T. Tan, Ph.D.[1,3], **Lisa J. Wilmes, Ph.D.**[2], **Bonnie N. Joe, M.D. Ph.D.**[2], **Natsuko Onishi, M.D. Ph.D.**[2], **Vignesh A. Arasu, M.D. Ph.D.**[2,4,5], **Nola M. Hylton, PhD.**[2], **Luca Marinelli, Ph.D.**[1], **David C. Newitt, Ph.D.**[2]

[1]GE Global Research, Niskayuna, NY, USA

[2]Department of Radiology and Biomedical Imaging, University of California, San Francisco, CA, USA

[3]Department of Radiology and Imaging, Hospital for Special Surgery, New York, NY, USA

[4]Department of Radiology, Kaiser Permanente Medical Center, Vallejo, CA, USA

[5]Division of Research, Kaiser Permanente Northern California, Oakland, CA, USA

Abstract

Background: Multi-b-valued/multi-shell diffusion provides potentially valuable metrics in breast magnetic resonance imaging (MRI) but suffers from low signal-to-noise and has potentially long scan times.

Purpose: To investigate the effects of model-based denoising with no loss of spatial resolution on multi-shell breast diffusion MRI; to determine the effects of down-sampling on multi-shell diffusion; and to quantify these effects in multi-b-valued (three directions per b-value) acquisitions.

Study Type: Prospective ("fully-sampled" multi-shell) and retrospective longitudinal (multi-b).

Subjects: One normal subject (multi-shell) and ten breast cancer subjects imaging at four time-points (multi-b).

Field Strength/Sequence: 3T multi-shell acquisition and 1.5T multi-b acquisition.

Assessment: The "fully-sampled" multi-shell acquisition was retrospectively down-sampled to determine the bias and error from down-sampling. Mean, axial/parallel, radial diffusivity, and fractional anisotropy (FA) were analyzed. Denoising was applied retrospectively to the multi-b-valued breast cancer subject dataset and assessed subjectively for image noise level and tumor conspicuity.

Statistical Tests: Parametric paired t-test ($p < 0.05$ considered statistically-significant) on mean and coefficient of variation of each metric – the apparent diffusion coefficient (ADC) from all

Correspondence: Ek T. Tan, Ph.D., Department of Radiology and Imaging, Hospital for Special Surgery, New York, NY, USA, Phone: 212-774-7601, Fax: 212-774-7830, tane@hss.edu.

b-values, fast ADC, slow ADC and perfusion fraction. Paired and two-sampled t-tests for each metric comparing normal and tumor tissue.

Results: In the multi-shell data denoising effectively suppressed FA (−45% to −78%), with small biases in mean diffusivity (−5% in normal, +23% in tumor, and −4% in vascular compartments). In the multi-b data, denoising resulted in small biases to the ADC metrics in tumor and normal contralateral tissue (by −3% to +11%), but greatly reduced the coefficient of variation for every metric (by −1% to −24%). Denoising improved differentiation of tumor and normal tissue regions in most metrics and time-points; subjectively, image noise level and tumor conspicuity were improved in the fast ADC maps.

Data Conclusion: Model-based denoising effectively suppressed erroneously high FA and improved the accuracy of diffusivity metrics.

Keywords

Denoising; diffusion imaging; breast imaging

INTRODUCTION

For decades, diffusion-weighted imaging (DWI) has been known to be sensitive to tissue microstructural and perfusion changes. In oncology, DWI-based biomarkers have been proposed to provide non-contrast-enhanced, quantitative information for tumor detection and staging, and for depicting changes due to treatment (apoptosis and necrosis)(1). Specifically, in breast cancer imaging, DWI can provide additional quantitative tumor characterizations (eg. hyper-cellularity and hyper-vascularization) that are complementary to the morphology and uptake dynamics provided by standard contrast-enhanced MRI(2, 3). To that end, single b-value-encoded DWI, as well as multi-b-valued DWI acquisitions with three or fewer diffusion-directions per b-value, have become routine add-on sequences in breast MRI exams. In clinical trials involving DWI(4), more advanced diffusion acquisitions may provide additional parameters for quantitative analysis. These acquisitions may utilize a greater number of scan directions, longer scan time, and more advanced modelling techniques such as intravoxel incoherent motion (IVIM)(5, 6) that provides both diffusion and perfusion metrics. Reduced mean diffusivity has been observed in hyper-cellular, malignant lesions; and changes in perfusion fraction have been hypothesized to occur due to tumor angiogenesis. While diffusion tensor imaging (DTI), which requires six or more diffusion-directions, is more routinely used in brain and peripheral nerve imaging, its use in breast MRI has been limited. This is due in part to the much lower diffusional anisotropy in breast parenchyma(7). Studies using DTI to obtain fractional anisotropy (FA) have found differentiation of tumors from normal tissue(7), and benign tumors from malignant tumors(8, 9); however, these studies have had conflicting results in determining the additional value of DTI over standard DWI in differentiating benign from malignant tumors.

While multi-b-valued DWI and DTI acquisitions can provide additional information for breast tumor characterization, they require significantly longer scan times, proportional to both the number of b-values and number of directions per b-value. In neuroimaging, multi-

shell diffusion imaging(10, 11) using multiple b-values and tens to hundreds of directions per b-value has become routinely utilized, especially in research applications. With multiple b-values and multiple directions per b-value, these multi-shell acquisitions can provide anisotropy measures as well as higher-order diffusional metrics such as diffusional kurtosis (12, 13), neurite density(14), and axonal diameter(15); the premise is that these anisotropy and higher-order metrics provide improved depiction of the underlying tissue characteristics. Furthermore, acquiring additional low b-value diffusivity provides perfusion fraction, which can be a differentiating diffusivity biomarker for treatment response (16) and potentially differentiate malignant from benign tumors (6) due to differences in the underlying tissue vascularity.

The application of multi-shell diffusion acquisition in breast imaging may provide similar benefits, but has been less popular for several reasons. In addition to the longer scan time, breast DWI typically has increased B0-susceptibility effects (distortion and blurring) due to proximity to the large chest cavity. There are also SNR challenges from poor B1 homogeneity, and additional bulk-motion and eddy-current effects that result in mis-registration that biases diffusivity results. Together, these challenges make higher-order diffusivity maps more susceptible to image and fitting noise, which can lead to reduced interpretability of diffusion maps and to quantitative inaccuracy of the calculated metrics. For example, it has been well-established that fractional anisotropy (FA) will be erroneously overestimated when SNR<25(17). In breast DWI, these effects are especially acute in regions with fatty tissue that are signal-suppressed by either fat saturation pulses or spectral-spatial water excitation, and in tissue boundary regions that are susceptible to mis-registration artifacts.

While many approaches to address B0-susceptibility (18, 19), B1-inhomogeneity (20) and registration challenges (21) have been made in breast DWI, DWI remains an inherently SNR-limited technique because of the high sampling bandwidth of the fast EPI readout. To address the SNR limitations, it may be desirable to apply denoising. Denoising typically relies on statistics obtained from a neighborhood of pixels, to tease out compartments for true signal vs. noise via iterative optimization techniques. Approaches using non-central chi/Rician noise distributions for signal magnitude (22), as well as Gaussian distribution for complex data (23) to reduce the thermal noise have been proposed. While these methods do improve the image quality, SNR and diffusivity metrics obtained, they utilize spatial kernels that invariably cause spatial smoothing and consequently compromised spatial resolution. Another promising approach utilizing principal components analysis (24) also uses kernels, but is more robust to smoothing as no explicit assumptions are made about edges and smoothness; this approach has been extended recently to include denoising of individual coil channels (25) with promising results. However, distortions and motion result in mis-registration of diffusion images, which can cause strong signal biases that can potentially be interpreted as signal rather than artifact. Another recent denoising approach instead utilizes multi-compartment diffusivity signal models (26). Here, denoising is applied only in the diffusion direction, so there is no spatial kernel and hence no trade-offs in terms of spatial resolution. This approach utilizes multiple compartments and is applicable primarily to multi-b-valued diffusion acquisition. It has shown promising results in removing outliers

in diffusion kurtosis imaging in the brain, as well as in improving nerve conspicuity in peripheral nerve imaging(27).

The goal of this work was to adapt the model-based diffusion denoising technique (26), for breast DWI, where the diffusivity, anisotropy and type of signal compartments are inherently different compared to the brain. Multi-shell diffusion (with more than six directions in a given shell) breast MRI acquisition was used to (i) more broadly determine the effects of denoising on both mean diffusivity and fractional anisotropy. Also, (ii) the effects of down-sampling by reducing the number of diffusion-encoding directions were evaluated. Multi-b-valued DWI with only three directions per b-value from a breast cancer patient cohort were denoised retrospectively, to (iii) quantify the effects of denoising on diffusivity and perfusion metrics, determine if denoising improves the separability of tumor from normal tissue, and determine if denoising improved linear fitting of longitudinal tumor metrics.

METHODS

Model-based denoising: breast DWI

The model-based diffusion denoising method(26) had been proposed with multi-shell diffusion brain MRI to provide 3–4 times acceleration and improved diffusivity maps. Because the algorithm is applied on a pixel-by-pixel basis across the diffusion directions, there is no possibility for any loss in spatial resolution. The method uses a generalized, multi-compartment model with $J \times N$ anisotropic and K isotropic tissue fractional compartments (f_{aniso}, f_{iso}), whereby the N anisotropic diffusion directions are predefined similar to those used in spherical deconvolution (28, 29). Each of the J anisotropic compartments have pre-defined axial/parallel and radial/orthogonal diffusivities $(\lambda_\parallel, \lambda_\perp)$, whereas each of the K isotropic compartments has just a mean diffusivity (λ) defined. For a maximum b-value, b and for each normalized gradient vector q, the model's signal estimate ($\hat{s}$) is defined as

$$\hat{s}(b,q) = \sum_{j=1}^{J} \sum_{n=1}^{N} f_{aniso,\,j,\,n} \exp\left(-\left(\lambda_{\parallel,\,jb}(q^T u_n)^2\right)\left(\lambda_{\perp,\,jb}\left(1 - (q^T u_n)^2\right)\right)\right) + \sum_{k=1}^{K} f_{iso,\,k} \exp(-\lambda_k b).$$

(1)

To adapt the method for breast multi-b diffusion, where tissue anisotropy is less than that in the brain and where fewer diffusion-encoding directions are typically used, a model with far fewer compartments ($J=1$, $K=20$) and reduced anisotropy ($N=40$) was proposed. In multi-b-valued acquisition, b-values smaller than the maximum b-value are created by q-vectors with a squared magnitude that is less than one. The composition of the compartments and optimization parameters for denoising are described in Table 1. The anisotropic compartment was approximated as normal fibroglandular tissue (NFT), and isotropic compartments as tumor, vascular and fat using mean diffusivity and fractional anisotropy (FA) values surveyed in the literature (6, 7, 30) as a guide, whereby NFT has

been reported to be more anisotropic than tumor tissue. The assumed fractional anisotropy (0.8) in the model was higher than that reported in the literature for NFT (~0.3); this approach parallels that used for spherical deconvolution in the brain (assumed FA=1 vs. actual white matter FA ~ 0.6–0.9), since the summation of many anisotropic compartments would lower the net anisotropy.

As a by-product of the model, the sum of fractional values belonging to each compartment could provide future utility for quantification and visualization of the total fraction of diffusion signal from each compartment, as shown in Fig. 1. These compartments parallel the restricted (R), hindered (H) and free (F) compartments used typically in models of the brain (31, 32), albeit obtained with different ranges of diffusivity and anisotropy.

Imaging: Multi-shell DWI

To determine the potential for applying the denoising algorithm for accelerating a multi-shell breast DWI acquisition by utilizing fewer multi-shell directions, a "fully-sampled" 30-directions acquisition was performed prospectively on a normal subject, age 58 years, on a 3T MRI system (Signa Premier, GE Healthcare, Chicago, IL, USA) using a 16-channel breast coil (InVivo, Gainesville, FL, USA), 128×104 matrix, slice thickness=3 mm, TR/TE=4460/59.7 ms, number of averages/shots=2/2, scan time=10 minutes. The b-values (and number of directions per b-value) were 100 sec/mm^2 (3 directions), 600 sec/mm^2 (11 directions), and 800 sec/mm^2 (16 directions). The data was retrospectively down-sampled to 12–29 directions total to determine the effects of denoising at different direction counts. Down-sampling was done by removing selected b=600 sec/mm^2 and b=800 sec/mm^2 data while approximately preserving the ratio of b=600:800 sec/mm^2. This allowed for at least six diffusion directions to be acquired in the b=800 sec/mm^2 shell directions (out of a total of 12 directions in the most down-sampled case), which was necessary for computing the diffusion tensor at the highest b-value. The b=100 sec/mm^2 data was excluded from down-sampling as there were only 3 directions in that shell. Because the diffusivity directions were generated with random seeding followed by charge dispersion per-shell (33) and then across all shells, the down-sampling could be considered to be random and adequate for resolving the diffusion tensor, with the exception of 12-direction data (see Discussion). Besides, breast tissue is not considered to be highly anisotropic as compared to white matter fiber bundles which require far more diffusion-encoding directions for resolving fiber crossings. The diffusivity maps calculated included mean diffusivity (MD), axial/parallel diffusivity (PD), radial diffusivity (RD) and fractional anisotropy (FA).

Multi-b DWI in breast cancer subjects

Denoising analysis was performed on multi-b DWI acquisitions from a subset of ten patients enrolled at one site of the ACRIN 6698 trial. (34) ACRIN 6698 was HIPAA-compliant and performed under individual site IRB approval, and all patients gave informed consent prior to enrolling. Inclusion criteria included biopsy-confirmed diagnosis of stage II–III invasive breast cancer and clinically or radiologically measurable disease in the breast with a tumor longest diameter (LD) >2.5 cm. For our 10 subject cohort age ranged from 35 to 66 years (median age = 47 years) and pre-treatment enhancing lesion size measured by dynamic contrast-enhanced (DCE)-MRI functional tumor volume (FTV) ranged from 4.8

– 119.9 cc (median FTV=12.0 cc). Each subject underwent 4 MRI studies over the course of neoadjuvant chemotherapy (NAC) for invasive breast cancer (T0: pre-NAC, T1:after 3 weeks NAC, T2: after 6 weeks NAC, T3: post NAC/pre-surgery). The acquisitions were obtained from a 1.5T scanner (Signa HDx, GE Healthcare, Waukesha WI) with one b=0 acquisition and three-directions per b-value={100, 600, 800} sec/mm^2, FOV=34–35 cm, slice thickness=4 mm, TR/TE=7500/67.6–67.9 ms. The analyzed metrics included: ADC (utilizing b=0 and all b-values), ADC_{slow} (b>0 data), ADC_{fast} (b=0 and 100 only), and perfusion fraction(16). With only three orthogonal diffusion directions per b-value the diffusion tensor (and hence FA) could not be obtained. Tumor and contralateral NFT were manually segmented using the original mono-exponential ADC maps and the b = 800 sec/mm^2 directional images. To reduce spatial-bias of diffusivity in large FOV breast imaging, gradient nonlinearity correction was applied(4).

Statistical Analysis

To compare undenoised vs denoised results, parametric paired t-test (p<0.05 for statistical significance) was performed on the mean difference and coefficient of variation (CV) of each metric; the hypotheses are that denoising does not bias diffusion metrics, and will reduce the CV (due to improved precision).

To evaluate whether denoising improved separability of tumor and NFT, a paired t-test was used to compare every metric (p<0.05 indicating significance); the hypothesis was that denoising would increase the separability of tumor and NFT metrics. This was tested across all time-points (N=40) and for every time-point (N=10). In addition, a two-sample t-test at each time-point (N=10) was performed to determine if the separability of tumor and NFT could also be observed when the subjects were pooled. To evaluate whether denoising might alter the longitudinal interpretability of diffusivity only in the tumors, a linear fit of each metric to the elapsed time from baseline was performed (constant + rate × elapsed time from baseline scan); the hypothesis was that denoising would not alter the fit, but would increase the R-squared value under the assumption that tumor diffusivity metrics underwent a monophasic change following neoadjuvant chemotherapy.

For subjective assessment, three radiologists with 9 to 18 years of experience reading breast MRI scans rated the ADC_{slow}, ADC_{fast} and perfusion fraction images from the first time-point for two metrics - image noise level and tumor conspicuity. Scores of −1, 0 and +1 were used to indicate preference for undenoised, no preference, and preference for denoised images respectively. DWI images from two of the subjects were used for training and calibration among the three readers. Assessments were performed independently by all three readers on the remaining 8 subjects in a different randomized order. A central slice depicting the tumor was chosen, and the undenoised and denoised image maps were presented (also in a randomized order) to the readers along with co-localized T1-weighted post-contrast-enhanced and subtraction images from the DCE acquisition. The mean scores and 95% confidence interval (CI) were computed for each image and metric. To determine inter-rater agreement, Fleiss' κ (considering classification only) and Kendall's coefficient of concordance (considers both classification and ordinality) were used, grouping results by metric because of the small dynamic range of the scores. Interpretation was as follows:

<0 indicated poor agreement, 0.01–0.20 slight agreement, 0.21–0.40 fair agreement, 0.41–0.60 moderate agreement, 0.61–0.80 substantial agreement, and 0.81–1.00 almost perfect agreement.

RESULTS

Effects from down-sampling and denoising on multi-shell diffusion

Fig.2 shows the effects of denoising at three sampling factors: full-sampling (30-directions), and down-sampling to 21-directions and 12-directions. The plots reflect the voxel-wise distribution of the diffusivity metrics due to denoising for each of the three compartments – NFT, tumor and vascular. To aid in visualizing each compartment, pixels belonging primarily to each compartment (with fractions exceeding 0.8 in the NFT compartment, 0.3 in the tumor compartment, or 0.8 in the vascular compartment) were colored in red, green or blue, respectively. On aggregate, denoising in the "fully-sampled" data resulted in a mostly proportional distribution of MD, PD and RD, with some extent of skewing towards a negative bias in NFT and vascular, and positive bias in tumor. In all three compartments, denoising reduced FA. With the 21-direction data, the same effects were observed, except that the spread and skew of the distributions were increased. With the 12-directions data, there were further increases in the spread of the distributions, along with a pronounced bias in the vascular FA to about 0.4–0.6.

Fig.3 shows the quantitative differences between denoised and undenoised metrics for each of the compartments, and at all of the tested number of diffusion directions (12 to 30). Denoising on the "fully-sampled" resulted in varying levels of bias in the diffusivity metrics. In MD the bias was −4.9% for NFT, +22.7% for tumor, and −3.5% for vascular; in PD the biases were all negative and were −18.4% for NFT, −11.7% for tumor, and −14.2% for vascular; in RD the biases were positive and were +6.9% for NFT, +45.6% for tumor, and +3.6% for vascular. As a result of the negative bias in PD and positive bias in RD, denoising resulted in significantly large negative biases in FA in all compartments (−44.9% for NFT, −78.2% for tumor, and −65.9% for vascular). With decrease in the number of diffusion directions, the trend for changes in bias (mean difference) and precision (standard deviation) appeared to be gradual, with bias not necessarily always increasing but precision was almost always reduced (standard deviation increased). However, at 12-directions there was a pronounced departure from the gradual trends in both bias and precision of most metrics; notably a flip in the polarity of the bias in MD of NFT (+6.1%), a close to zero bias in RD in all three compartments, and a reversal in the trend of FA suppression in the vascular compartment.

Fig.4 shows the error resulting from all down-sampling factors in all four metrics and fractional compartments, with the denoised "fully-sampled" data as a reference. In all metrics (MD, PD, RD and FA) standard deviation increased with down-sampling. However, the biases introduced by down-sampling in MD, PD, and RD for the NFT and tumor compartments were small (<5%). The same metrics in the vascular compartments had larger biases (>5%). The magnitudes of the changes in FA bias and precision were larger than those in MD, PD and RD. The errors in the resulting compartment fractions were also compared; the biases from down-sampling were small in the restricted (NFT, <6%) and free

(vascular, <2%) compartments, and were somewhat larger in the hindered (tumor, <20%) compartment. Interestingly, in all three compartments, the errors in compartment fraction changes had very high precision (small standard deviations) relative to the magnitudes of the biases.

Fig.5 shows the breast DWI maps before and after denoising, with 12-directions (down-sampled) and with 30-directions (fully-sampled). The quantitative effects on the diffusivity metrics, especially in FA, could be observed by comparing the undenoised and denoised images.

Multi-b DWI in breast cancer subjects

As summarized in Table 2, denoising resulted in very small changes (<3%) to ADC and ADC_{slow} for tumors (increase) and contralateral NFT (decrease), with the polarity of the bias in ADC the same as that of MD in the multi-shell data analysis. Denoising increased ADC_{fast} by +11.4% and +9.9% in tumor and NFT respectively. Denoising increased the perfusion fraction by 12.5% in tumor and 36.9% in NFT, but the values for perfusion fractions were small to begin with (0.075, 0.057 in tumor and NFT respectively). For every metric and in both tumors and NFT, the coefficient of variation (CV) within the ROIs were significantly reduced ($p<0.001$). In particular, the CV reduction was substantial in both ADC_{fast} (−12.7% to −14.3%) and perfusion fraction (−18.0% to −24.4%).

Fig.6 shows diffusivity maps from one subject, which compare the effects of denoising on ADC, ADC_{slow} and perfusion fraction maps. The arrows in Fig. 6 point to vascular structures on the undenoised and denoised ADC_{fast} and perfusion maps.

Table 3 summarizes results aggregated from all time-points. In every metric, paired t-tests show that tumor metrics were significantly different from NFT metrics in both denoised and undenoised maps. This was despite denoising not always increasing the absolute difference between tumor and NFT (ADC and ADC_{slow}). However, the p-values were always lower in denoised than undenoised; in particular, the perfusion fraction p-value was 0.01 undenoised and <0.001 denoised.

In the longitudinal analysis (also in Table 3), ADC and ADC_{slow} had small linear rates (~2.1 μm^2/s/day) with relatively low adjusted R-squared values (0.22–0.25) that didn't change much with denoising. For ADC_{fast}, denoising increased the temporal rate with a much larger increase in adjusted R-squared from 0.01 to 0.18. The adjusted R-squared values for perfusion was very small (0.02) and was further reduced by denoising.

Fig.7 shows the distribution of the metrics at each time point. In the paired t-tests, 12 of 16 metric time-points, NFT and tumor regions were significantly different in both denoised and undenoised. In 2 of 16 time-points (perfusion fraction T0 and T2), significant differences were only in the denoised maps. In 13 of 16 metric time-points, p-values were lower in denoised than in undenoised. The two-sample t-test results were similar to the paired t-tests, except that 12 of 16 metric time-points had lower p-values in denoised than undenoised.

For the subjective assessments, the readers preferred the image noise level in the denoised ADC_{fast} image (mean: +0.96, 95% confidence interval or CI: +0.87 to +1.0) but preferred

the undenoised ADC_{slow} (mean: −0.46, 95% CI: −0.71 to −0.21) and perfusion fraction images (mean: −0.67, 95% CI: −0.99 to −0.35). Tumor conspicuity was preferred in the denoised ADC_{fast} (mean: +0.33, 95% CI: +0.13 to +0.54) and was neutral in both ADC_{slow} (mean: −0.08, 95% CI: −0.20 to +0.04) and perfusion fraction (all readers rated 0). The inter-rater agreement for image noise level was moderate (κ=0.53, p<0.001) to almost perfect when ordinality was considered (concordance=0.86, p<0.001); for tumor conspicuity it was fair (κ=0.21, p=0.04) to moderate (concordance=0.52, p=0.04).

DISCUSSION

A model-based denoising scheme for breast DWI was demonstrated in multi-shell and multi-b-valued acquisitions. The denoising scheme was shown to be highly effective at suppressing erroneously high FA without compromising spatial resolution, similar to that observed in multi-shell diffusion denoising in the peripheral nerves(27). In this breast DWI work, the FA reductions were particularly conspicuous in the fatty tissue regions with low signal due to fat-suppression and in tissue boundary regions (fat-air, fat-NFT interfaces for instance). Erroneously high FA bias is a common DTI post-processing issue(35), especially in tissue boundary regions where misregistration due to either motion or eddy currents can severely bias FA calculation. Unlike denoising of additive thermal noise, where methods that offset noise-bias or PCA-denoising may apply(24), such misregistration artifacts are more like measurement outliers. These are more suited to correction by the proposed model-based technique used here. When combined with PCA-based denoising(27), the model-based denoising could provide a powerful means for correcting both additive noise and outlier artifacts to improve quantitative analysis and visualization of diffusivity maps.

Another important result from this work was the demonstration of reduced coefficient of variation in every diffusivity metric, especially ADC_{fast} and perfusion fraction in the multi-b-valued DWI cohort. On its own, a reduced coefficient of variation may imply that denoising either improved precision, or that it homogenized the metrics; which in turn might result in tumor and NFT metrics becoming less differentiable. The results of this work suggest that the former was the more likely situation. This is because in comparing tumor and NFT regions in the patient multi-b-valued acquisitions, the statistical separation between tumor and NFT was increased by the denoising technique in almost every metric and on a per-subject and per-time-point basis, even when the mean differences between the metrics were unchanged. In addition, the improved separation between tumor and NFT could imply that denoising could improve large cohort tumor characterization studies. The precision-improving effects of denoising were particularly noted in ADC_{fast} and the perfusion fraction, which require multi-b-valued acquisitions and were typically very noisy. Subjectively, denoising improved the ADC_{fast} maps in both image noise level and tumor conspicuity. Although the subjective results were mixed (perceived noise levels in ADC_{slow} and perfusion maps were lower), it is likely due to the subtle effects and lack of strong anatomical features in the diffusion maps. Although not subjectively evaluated, the improved coefficient of variation in ADC_{fast} and perfusion fraction may provide improved visualization of mammary vessels, as well detection of microvasculature components that could be used to separate malignant from benign tumors.

Another potential benefit of denoising is better characterization of tumor response to chemotherapy through longitudinal breast DWI studies. For example in the ACRIN 6698 Trial, mean tumor ADC demonstrated excellent repeatability(36) but it provided only moderate power for predicting treatment outcome(34). While the current work was not powered for investigating treatment effects, we did observe that linear fitting of the longitudinal data was improved by denoising for ADC_{fast}; the adjusted R-squared value was improved by a factor of ten. A simple linear fit was applied as only four time points were available in this retrospective cohort, and due to the lack of any a-priori expectations for the longitudinal behavior of the different investigated metrics. In this work it was observed that the longitudinal pattern of diffusivity change was only mildly temporally-linear in ADC and ADC_{slow}.

Denoising on both multi-shell and multi-b DWI resulted in some bias in the diffusivity metrics. In particular, the application of denoising resulted in a larger observed bias in multi-shell MD than that in the multi-b DWI ADC, albeit the biases were both negative. MD and ADC could be deemed comparable as they were both isotropic diffusivity measures utilizing all available b-values. The primary reason for the disparity in bias was likely not fundamental, but rather due to differences in the segmentation techniques in the two analyses: in the multi-b DWI careful manual segmentations of both tumor and NFT were performed, whereas in the multi-shell data all pixels were included. The latter processing would include noisy regions with low signal intensities and regions with misregistration artifacts, which would likely increase the denoising-related bias. A secondary factor was that higher b-values were weighted more heavily in the multi-shell acquisition vs. equal weighting across all b-values in the multi-b DWI. This reasoning was supported by the observation of higher precision (lower standard deviation) in the fractional compartments when the number of diffusion-encoding directions were reduced; this implied the differences due to down-sampling were caused by the diffusion data itself rather than by the denoising model. Furthermore, previously reported comprehensive simulations(26) demonstrated that this denoising scheme did not bias diffusivity measurements.

A benefit of multi-shell diffusion acquisitions is the ability to derive both the isotropic metrics, such as ADC_{slow}, ADC_{fast}, and perfusion fraction, and the metrics associated with the diffusion tensor (FA, PD, RD, etc.). The longer scan time of the multi-shell acquisition over 3-direction DWI could be addressed by applying denoising to multi-shell data with fewer diffusion directions. With the b-values chosen in this work, a 13 direction multi-shell acquisition with three b=100, four b=600 and six b=800 directions would avoid the situation of the outer shell having only five directions, which would be numerically inadequate for resolving the six elements in the diffusion tensor, even though all b-values were utilized in our diffusion fit. With 13 total diffusion directions, the scan time with the same multi-shell parameters would be under 4.25 minutes (as compared to the ten minute fully-sampled scan). Further acceleration by a factor of about two could be achieved with simultaneous multi-slice(37), allowing the acquisition of additional b-values to provide improved fitting for investigation of intravoxel incoherent motion metrics.

The model-based denoising also provides fractional values of the modelled tissue compartments, which could provide useful visualization and quantification. As an example,

signal from NFT, tumor or vascular could be visualized separately (Fig. S1). For quantification, the tumor compartment and vascular compartment could be used for segmentation and also to indicate the likelihood for malignant angiogenesis. For future work, the vascular compartment from denoising could also be compared to perfusion fraction obtained by fitting.

Limitations

In this work, there were several study design limitations. Firstly, no fully-sampled multi-shell tumor data was acquired because of the long scan time, so the down-sampling effects on the tumor compartment were not validated. Secondly, because this was an entirely retrospective study, the parameters used in the data were not optimized and limited the interpretability of the comparisons that were made. For instance, two multi-b-schemes were acquired; a multi-shell for the down-sampling evaluation, and multi-b DWI for the patient cohort analysis. Also, the effects of down-sampling were determined on 3T data while the multi-b was acquired at 1.5T. More importantly, because this was retrospective, optimized accelerated multi-shell patient data was not acquired. Therefore, the possibility for scan time reduction was not experimentally validated. A prospective study design would also have allowed for collection of complex raw data that could have allowed for removal of Rician noise bias, rather than the magnitude coil-combined image data in this study.

Another limitation of this study was that the NFT ROIs were not segmented in the fully-sampled multi-shell data to compare against the NFT ROIs from the multi-b DWI. This was done to satisfy the goal of including a majority of pixels for analysis in the multi-shell data in order to more fully quantify the effects of down-sampling from the fully-sampled dataset, rather than using only on a small subset of pixels selected manually to characterize NFT and tumor ROIs. Furthermore, to maintain consistency in the analysis, the classification for pixels were kept constant (classified from the fully-sampled case).

The clinical utility of the denoising technique was not demonstrated in this work. For instance, trace-weighted images, the most commonly available DWI, were not analyzed. Also, the analysis of the longitudinal data was not compared against dynamic contrast-enhanced breast MRI or with the knowledge of the tumor type or outcome from the chemotherapy. Therefore, the assumption of a monophasic linear longitudinal change was merely to evaluate improvements made by denoising to the longitudinal stability of the diffusion measurements. Future work would utilize an optimized 13 directions multi-shell acquisition for longitudinal imaging of breast cancer subjects.

Alternative diffusion acquisition techniques may provide accelerated acquisition or higher-order diffusivity information. For example, q-space imaging(38) can reduce the number of diffusion directions by sampling multiple diffusivity directions; double-diffusion encoding(39) and oscillating gradient encoding(40) can provide length-scale selective information. Nevertheless, the advantages of applying the proposed denoising technique could be realized in any of these newer acquisition techniques, and more importantly could be realized via retrospective application to existing image data providing the individual diffusion direction images are available; complex coil-by-coil data that is seldom stored is not required.

CONCLUSION

In summary, an effective denoising method for multi-b-valued breast diffusion imaging was demonstrated, which could be used in conjunction with a multi-shell diffusion acquisition scheme to provide improved precision of diffusion tensor- and multi-b-based metrics.

Supplementary Material

Refer to Web version on PubMed Central for supplementary material.

Acknowledgements:

REFERENCES

1. Padhani AR, Koh D-M: Diffusion MR Imaging for Monitoring of Treatment Response.Magn Reson Imaging C2011; 19:181.

2. Zhang L, Tang M, Min Z, Lu J, Lei X, Zhang X: Accuracy of combined dynamic contrast-enhanced magnetic resonance imaging and diffusion-weighted imaging for breast cancer detection: a meta-analysis.Acta Radiologica Stock Swed 19872015; 57:651–60.

3. Zhang M, Horvat JV, Bernard-Davila B, et al.: Multiparametric MRI model with dynamic contrast-enhanced and diffusion-weighted imaging enables breast cancer diagnosis with high accuracy.J Magn Reson Imaging2018; 49:864–874. [PubMed: 30375702]

4. Newitt DC, Tan ET, Wilmes LJ, et al.: Gradient nonlinearity correction to improve apparent diffusion coefficient accuracy and standardization in the american college of radiology imaging network 6698 breast cancer trial.J Magn Reson Imaging2015; 42:908–19. [PubMed: 25758543]

5. Bihan DL, Turner R, MacFall JR: Effects of intravoxel incoherent motions (IVIM) in steady-state free precession (SSFP) imaging: application to molecular diffusion imaging.Magnetic Resonance in Medicine1989; 10:324337. [PubMed: 2733589]

6. Cho GY, Moy L, Kim SG, et al.: Evaluation of breast cancer using intravoxel incoherent motion (IVIM) histogram analysis: comparison with malignant status, histological subtype, and molecular prognostic factors.Eur Radiol2015; 26:25472558. [PubMed: 26615557]

7. Partridge SC, Ziadloo A, Murthy R, et al.: Diffusion tensor MRI: Preliminary anisotropy measures and mapping of breast tumors.J Magn Reson Imaging2010; 31:339347. [PubMed: 20099346]

8. Luo J, Hippe DS, Rahbar H, Parsian S, Rendi MH, Partridge SC: Diffusion tensor imaging for characterizing tumor microstructure and improving diagnostic performance on breast MRI: a prospective observational study.Breast Cancer Res Bcr2019; 21:102. [PubMed: 31484577]

9. Baltzer PAT, Schäfer A, Dietzel M, et al.: Diffusion tensor magnetic resonance imaging of the breast: a pilot study.Eur Radiol2010; 21:1–10. [PubMed: 20668860]

10. Aganj I, Lenglet C, Sapiro G, Yacoub E, Ugurbil K, Harel N: Reconstruction of the orientation distribution function in single- and multiple-shell q-ball imaging within constant solid angle.Magnet Reson Med2010; 64:554–566.

11. Descoteaux M, Deriche R, Bihan DL, Mangin J-F, Poupon C: Multiple q-shell diffusion propagator imagingq.Med Image Anal2011; 15:603. [PubMed: 20685153]

12. Jensen JH, Helpern JA, Ramani A, Lu H, Kaczynski K: Diffusional kurtosis imaging: the quantification of non-gaussian water diffusion by means of magnetic resonance imaging.Magnet Reson Med2005; 53:1432–40.

13. Hui ES, Cheung MM, Qi L, Wu EX: Towards better MR characterization of neural tissues using directional diffusion kurtosis analysis.Neuroimage2008; 42:122–34. [PubMed: 18524628]

14. Zhang H, Schneider T, Wheeler-Kingshott CA, Alexander DC: NODDI: Practical in vivo neurite orientation dispersion and density imaging of the human brain.Neuroimage2012; 61:1000. [PubMed: 22484410]

15. Assaf Y, Blumenfeld-Katzir T, Yovel Y, Basser PJ: AxCaliber: A Method for Measuring Axon Diameter Distribution from Diffusion MRI.Magnet Reson Med2008; 59:1347.

16. Lewin M, Fartoux L, Vignaud A, Arrivé L, Menu Y, Rosmorduc O: The diffusion-weighted imaging perfusion fraction f is a potential marker of sorafenib treatment in advanced hepatocellular carcinoma: a pilot study.Eur Radiol2011; 21:281–290. [PubMed: 20683597]

17. Jones DK, Basser PJ: "Squashing peanuts and smashing pumpkins": How noise distorts diffusion-weighted MR data.Magnet Reson Med2004; 52:979–993.

18. Hancu I, Govenkar A, Lenkinski RE, Lee S-K: On shimming approaches in 3T breast MRI.Magnet Reson Med2013; 69:862867.

19. Lee S-K, Tan ET, Govenkar A, Hancu I: Dynamic slice-dependent shim and center frequency update in 3 T breast diffusion weighted imaging.Magnet Reson Med2013; 71:18131818.

20. Hancu I, Fiveland E, Park K, Giaquinto RO, Rohling K, Wiesinger F: Flexible, 31-Channel breast coil for enhanced parallel imaging performance at 3T.Magnet Reson Med2015; 75:897905.

21. Hancu I, Lee S-K, Hulsey K, et al.: Distortion correction in diffusion-weighted imaging of the breast: Performance assessment of prospective, retrospective, and combined (prospective + retrospective) approaches.Magnet Reson Med2017; 78:247253.

22. Lam F, Babacan SD, Haldar JP, Weiner MW, Schuff N, Liang Z-P: Denoising diffusion-weighted magnitude MR images using rank and edge constraints.Magnet Reson Med2013; 71:12721284.

23. Haldar JP, Wedeen VJ, Nezamzadeh M, et al.: Improved diffusion imaging through SNR-enhancing joint reconstruction.Magnet Reson Med2012; 69:277289.

24. Veraart J, Novikov DS, Christiaens D, Ades-aron B, Sijbers J, Fieremans E: Denoising of diffusion MRI using random matrix theory.Neuroimage2016; 142:394406. [PubMed: 27523449]

25. Lemberskiy G, Baete S, Veraart J, Shepherd T, Fieremans E, Novikov DS: Achieving sub-mm clinical diffusion MRI resolution by removing noise during reconstruction using random matrix theory.Proc ISMRM2019:770.

26. Sperl JI, Sprenger T, Tan ET, Menzel MI, Hardy CJ, Marinelli L: Model-based denoising in diffusion-weighted imaging using generalized spherical deconvolution.Magnet Reson Med2017; 13:534.

27. Sneag DB, Zochowski KC, Tan ET, et al.: Denoising of diffusion MRI improves peripheral nerve conspicuity and reproducibility.J Magn Reson Imaging2019.

28. Tournier J-D, Yeh C-H, Calamante F, Cho K-H, Connelly A, Lin C-P: Resolving crossing fibres using constrained spherical deconvolution: Validation using diffusion-weighted imaging phantom data.Neuroimage2008; 42:617. [PubMed: 18583153]

29. Dell'Acqua F, Simmons A, Williams SCR, Catani M: Can Spherical Deconvolution Provide More Information Than Fiber Orientations? Hindrance Modulated Orientational Anisotropy, a True-Tract Specific Index to Characterize White Matter Diffusion.Hum Brain Mapp2012; 34:2464. [PubMed: 22488973]

30. Jiang R, Ma Z, Dong H, Sun S, Zeng X, Li X: Diffusion tensor imaging of breast lesions: evaluation of apparent diffusion coefficient and fractional anisotropy and tissue cellularity.Br J Radiology2016; 89:20160076.

31. Assaf Y, Basser PJ: Composite hindered and restricted model of diffusion (CHARMED) MR imaging of the human brain.Neuroimage2005; 27:48. [PubMed: 15979342]

32. Alexander DC: A General Framework for Experiment Design in Diffusion MRI and Its Application in Measuring Direct Tissue-Microstructure Features.Magnet Reson Med2008; 60:439.

33. Jones DK, Simmons A, Williams SCR, Horsfield MA: Non-invasive assessment of axonal fiber connectivity in the human brain via diffusion tensor MRI.Magnet Reson Med1999; 42:37–41.

34. Partridge SC, Zhang Z, Newitt DC, et al.: Diffusion-weighted MRI Findings Predict Pathologic Response in Neoadjuvant Treatment of Breast Cancer: The ACRIN 6698 Multicenter Trial.Radiology2018; 289:618–627. [PubMed: 30179110]

35. Polders DL, Leemans A, Hendrikse J, Donahue MJ, Luijten PR, Hoogduin JM: Signal to noise ratio and uncertainty in diffusion tensor imaging at 1.5, 3.0, and 7.0 Tesla.J Magn Reson Imaging2011; 33:1456–1463. [PubMed: 21591016]

36. Newitt DC, Zhang Z, Gibbs JE, et al.: Test-retest repeatability and reproducibility of ADC measures by breast DWI: Results from the ACRIN 6698 trial.J Magnetic Reson Imaging Jmri2018; 49:1617–1628.

37. Ohlmeyer S, Laun FB, Palm T, et al.: Simultaneous Multislice Echo Planar Imaging for Accelerated Diffusion-Weighted Imaging of Malignant and Benign Breast Lesions.Invest Radiol2019; 54:524–530. [PubMed: 30946181]

38. Westin C-F, Knutsson H, Pasternak O, et al.: Q-space trajectory imaging for multidimensional diffusion MRI of the human brain.Neuroimage2016; 135(C):345362. [PubMed: 26923372]

39. Finsterbusch J: Double-spin-echo diffusion weighting with a modified eddy current adjustment☆.Magn Reson Imaging2010; 28:434. [PubMed: 20071120]

40. Does MD, Gore JC: Compartmental study of diffusion and relaxation measured in vivo in normal and ischemic rat brain and trigeminal nerve.Magnet Reson Med2000; 43:837–844.
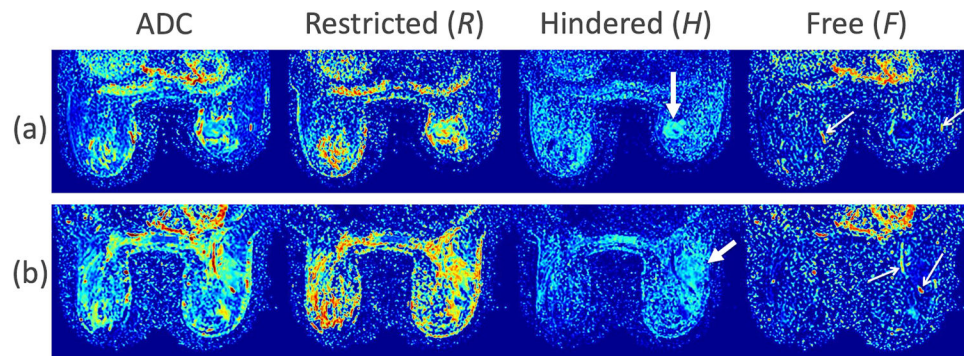
Figure 1.
Visualization of fractional compartments – restricted (normal fibroglandular tissue), hindered (tumor, thick arrows point to tumors) and free (vascular, thin arrows point to mammary vessels), in (a) subject 2 (66 yr., invasive ductal carcinoma [IDC], FTV=7.9 cc), and (b) subject 3 (37 yr., IDC, FTV=62.2 cc).
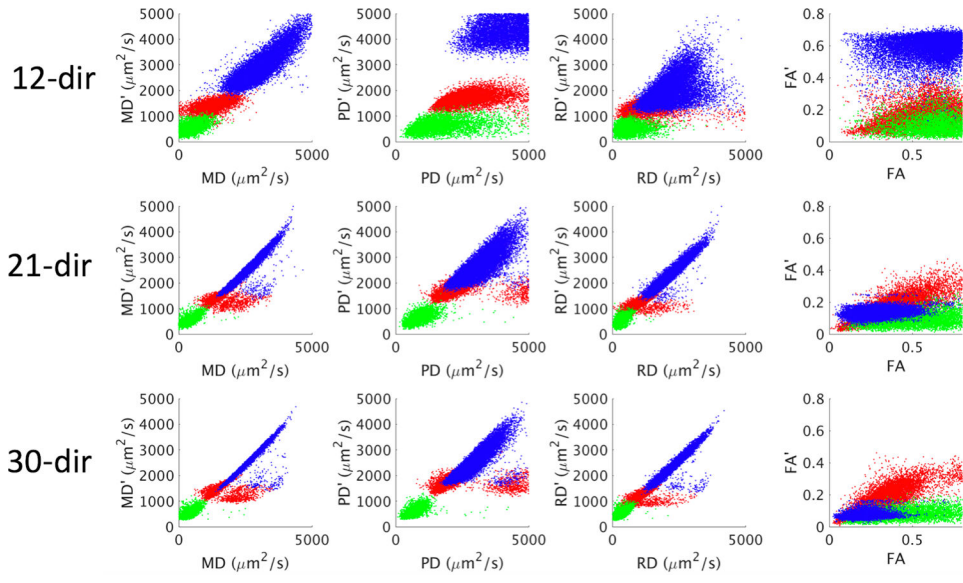
Figure 2.
Effects of denoising shown as scatterplots for 12-directions multi-shell (top row), 21-directions multi-shell (middle row) and 30-directions multi-shell. Each plot shows the denoised metric, MD' for instance vs. the original metric MD. The colors indicate pixels with fractional compartments being strongly anisotropic normal fibroglandular tissue (red), strongly isotropic tumor tissue (green), or strongly isotropic vascular (blue).
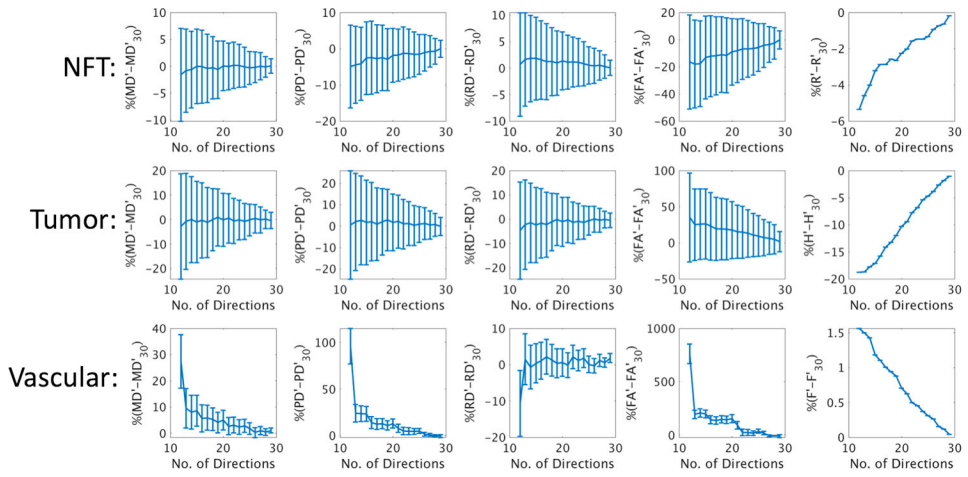
Figure 3.
Normalized differences between denoised and undenoised metrics for normal fibroglandular tissue (NFT, top row), tumor (middle row) and vascular (bottom row) compartments and at different down-sampled number of diffusion directions down from "fully-sampled" 30-directions data.
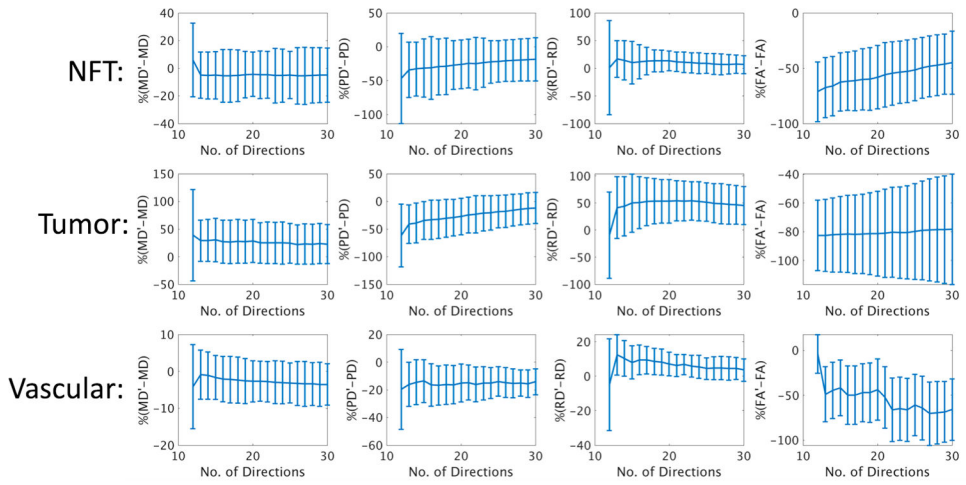
Figure 4.
Error of down-sampling against "fully-sampled" 30-directions multi-shell DWI in normal fibroglandular (NFT) compartment (top row), tumor compartment (middle row) and vascular compartment (bottom row). The MD, PD, RD and FA metrics are shown, as well as the compartment fractions for restricted (*R*), hindered (*H*) and free (*F*) diffusivity, which correspond respectively to the NFT, tumor and vascular compartments.
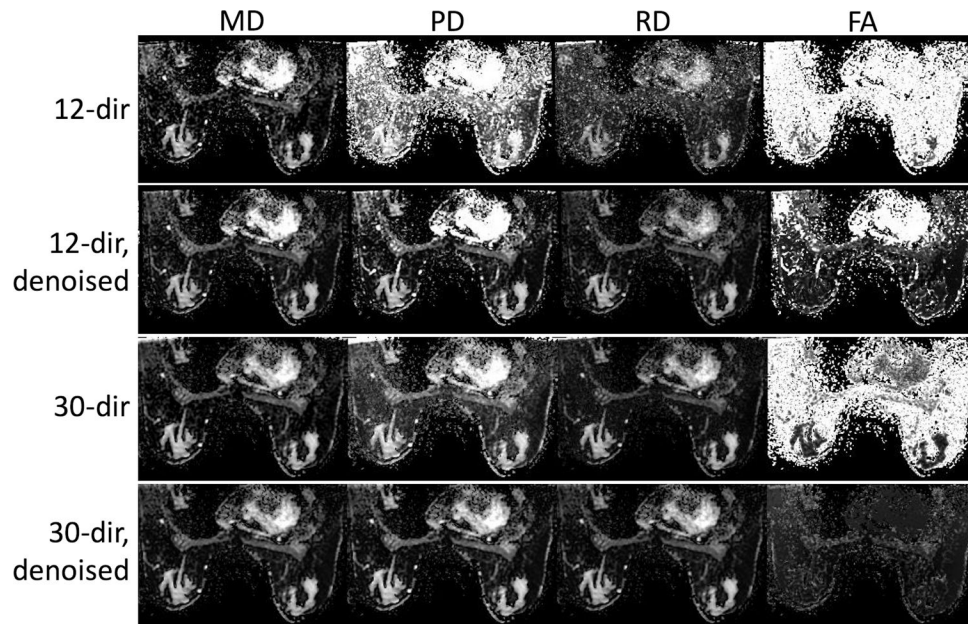
Figure 5.
Effects of denoising on multi-shell DWI images down-sampled to 12-directions (top rows) and fully-sampled at 30-directions (bottom rows), showing maps for mean diffusivity (MD), axial/parallel diffusivity (PD), radial diffusivity (RD) and fractional anisotropy (FA) in columns.
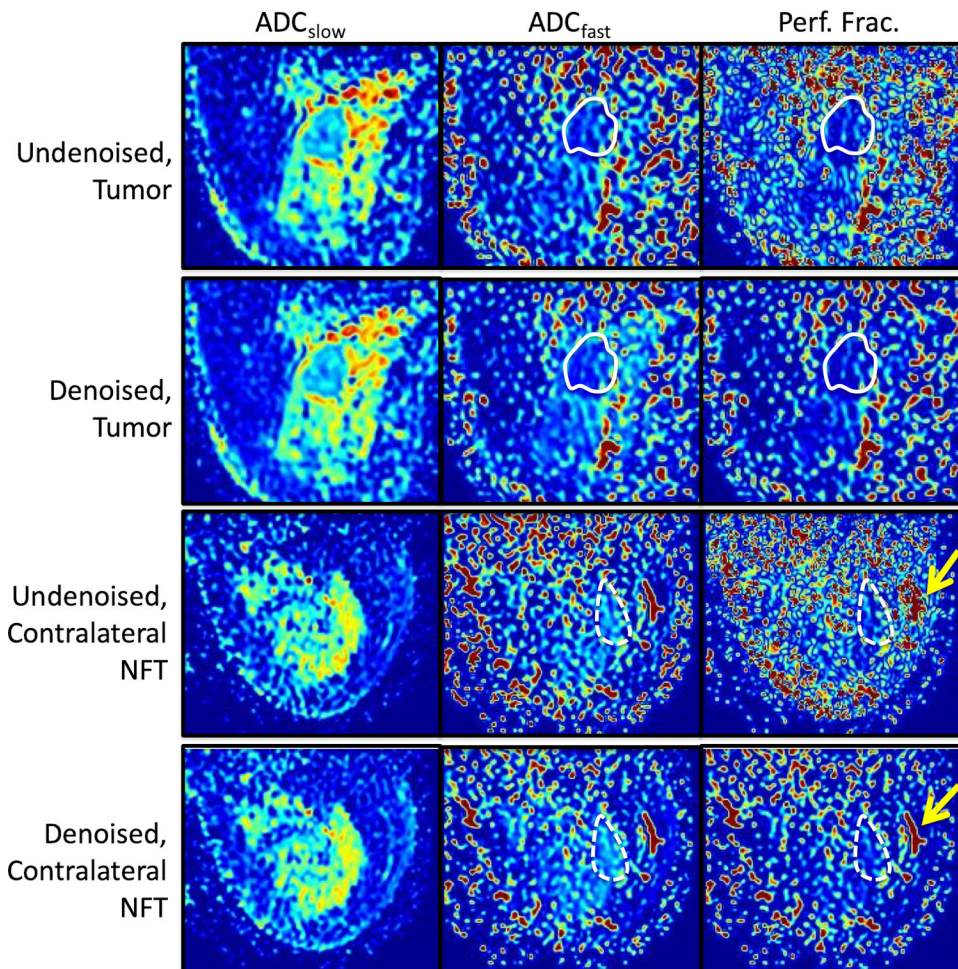
Figure 6.
Maps from subject 1 (57 yr., IDC, FTV=12.0 cc), standard and denoised, with segmented tumor (solid line) and contralateral fibroglandular tissue (dashed line), showing significant reduction in image texture and outliers in the b=100 sec/mm^2 and perfusion fraction maps. The lateral mammary vessel was better visualized after denoising (arrow).
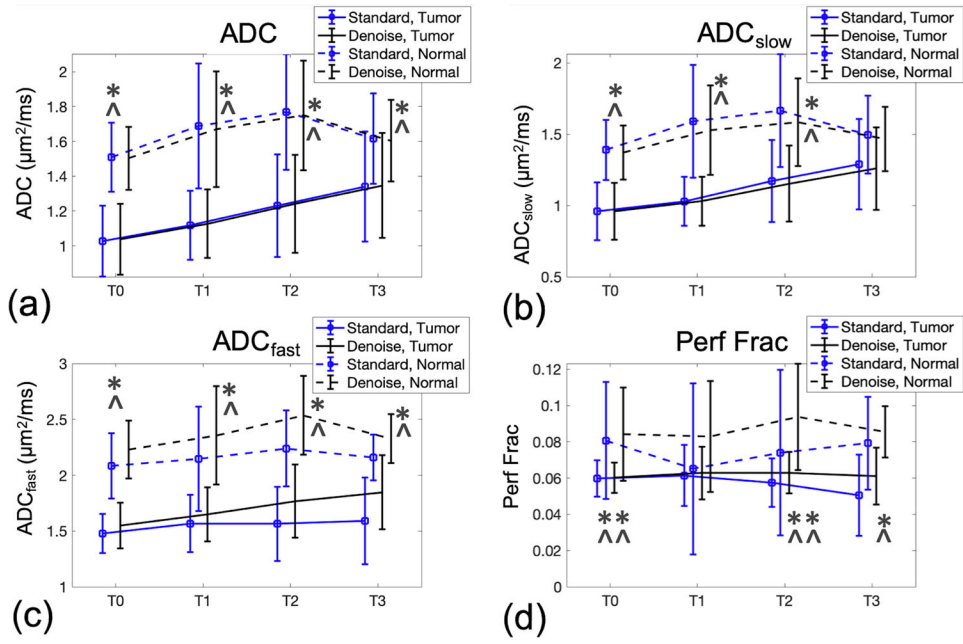
Figure 7.
Distribution (mean and standard deviation) across N=10 subjects across all four time-points (T0 to T3) in tumor and normal regions of interests, showing reduced variance in most metrics and time-points resulting from denoising. Statistically significant (p<0.05) paired t-test differences between tumor and normal regions in both undenoised and denoised are indicated with *, and statistically significant differences in denoised only are indicated with **. Two-sampled t-test differences are indicated with ^ (undenoised and denoised) and ^^ (denoised only).

Table 1.

Generalized, multi-compartment diffusion model for breast diffusivity with compartments J and N representing the number of assumed diffusivities and the number of directions respectively in anisotropic compartment, or K for the number of assumed diffusivities in isotropic compartments. In this work, the parameters for denoising optimization were number of iterations = 52, Nesterov's iteration parameter = 3.5.

Anisotropic or Isotropic	Tissue Compartment	Range of mean diffusivity ($\mu m^2/s$)	Fractional anisotropy	# Compartments ($J \times N$) or (K)
Anisotropic	Normal fibroglandular tissue (NFT)	1800	0.8	1×40
Isotropic	Tumor	400 to 2000	0.0	8
Isotropic	Vascular	2400 to 30000	0.0	8
Isotropic	Fat	50 to 300	0.0	4

Table 2.

Differences (denoising minus no denoising) in multi-b-value metrics of normal fibroglandular tissue (NFT) and tumors, and their coefficient of variation as compared statistically using the pair-wise, non-parametric Wilcoxon signed-rank test.

Metric	NFT			Tumor		
	Mean difference	% Mean difference (p-value)	%Change in CV (p-value)	Mean difference	% Mean difference (p-value)	%Change in CV (p-value)
ADC (b=0, 100, 600, 800)	$-14.7\ \mu m^2/s$	-0.7 (p=0.01)	-1.2 (p<0.001)	$+9.5\ \mu m^2/s$	-1.0 (p<0.001)	-0.7 (p<0.001)
ADC$_{slow}$ (b=100, 600, 800)	$-48.5\ \mu m^2/s$	-2.5 (p<0.001)	-2.7 (p<0.001)	$-12.0\ \mu m^2/s$	-0.8 (p=0.012)	-1.5 (p<0.001)
ADC$_{fast}$ (b=0, 100 only)	$+205\ \mu m^2/s$	$+9.9$ (p<0.001)	-12.7 (p<0.001)	$+154\ \mu m^2/s$	$+11.4$ (p<0.001)	-14.3 (p<0.001)
Perfusion fraction	$+0.012$	$+36.9$ (p=0.002)	-24.4 (p<0.001)	$+0.045$	$+12.5$ (p=0.003)	-18.0 (p<0.001)

Table 3.

Results from per-exam paired t-test of NFT minus tumor metrics (mean and p-value), and longitudinal analysis of tumor metrics with linear fitting (slope and adjusted R-squared value).

Metric	Paired t-test of NFT-Tumor					
	Undenoised			Denoised		
	NFT Mean	Tumor Mean	p-value	NFT Mean	Tumor Mean	p-value
ADC ($\mu m^2/s$)	1646$\mu m^2/s$	1179$\mu m^2/s$	<0.001	1631$\mu m^2/s$	1188$\mu m^2/s$	<0.001
ADC$_{slow}$ ($\mu m^2/s$)	1536$\mu m^2/s$	1113$\mu m^2/s$	<0.001	1488$\mu m^2/s$	1101$\mu m^2/s$	<0.001
ADC$_{fast}$ ($\mu m^2/s$)	2157$\mu m^2/s$	2362$\mu m^2/s$	<0.001	1550$\mu m^2/s$	1703$\mu m^2/s$	<0.001
Perfusion fraction	0.0748	0.0573	0.013	0.0867	0.0618	<0.001

Metric	Longitudinal Comparison (const + rate × time)					
	Undenoised			Denoised		
	const	rate	Adj. R-Squared	const	rate	Adj. R-Squared
ADC ($\mu m^2/s$)	1027	2.1/day	0.217	1039	2.1/day	0.221
ADC$_{slow}$ ($\mu m^2/s$)	952	2.2/day	0.246	956	2.0/day	0.230
ADC$_{fast}$ ($\mu m^2/s$)	1480	0.9/day	0.0143	1553	2.1/day	0.180
Perfusion fraction	0.061	−0.054/day	0.021	0.061	0.012/day	−0.022